ARTICLE OPEN

Symmetric carbon tetramers forming spin qubits in hexagonal boron nitride

Zsolt Benedek[1,2,3], Rohit Babar [1,2], Ádám Ganyecz [1,2], Tibor Szilvási[3], Örs Legeza[1,4], Gergely Barcza[1,2,3✉] and Viktor Ivády [2,5,6✉]

Point defect quantum bits in semiconductors have the potential to revolutionize sensing at atomic scales. Currently, vacancy-related defects are at the forefront of high spatial resolution and low-dimensional sensing. On the other hand, it is expected that impurity-related defect structures may give rise to new features that could further advance quantum sensing in low dimensions. Here, we study the symmetric carbon tetramer clusters in hexagonal boron nitride and propose them as spin qubits for sensing. We utilize periodic-DFT and quantum chemistry approaches to reliably and accurately predict the electronic, optical, and spin properties of the studied defect. We show that the nitrogen-centered symmetric carbon tetramer gives rise to spin state-dependent optical signals with strain-sensitive intersystem crossing rates. Furthermore, the weak hyperfine coupling of the defect to their spin environments results in a reduced electron spin resonance linewidth that can enhance sensitivity.

INTRODUCTION

Condensed matter physics in low dimensions is already a vast, yet rapidly growing field. Especially, transition metal dichalcogenides[1,2] and complex van der Waals heterostructures[3,4] develop with an unprecedented pace. The study of these nanometer-scale structures and related phenomena demands novel high spatial resolution sensing devices operating in a wide temperature range and sensitive to various external fields. Point defect quantum bits in semiconductors, such as the NV center in diamond[5,6] and the silicon vacancy in silicon carbide[7], have already demonstrated outstanding capabilities in high spatial-resolution sensing and fulfilled many of these requirements[8–12]. The distance of the sensor from the targeted system is of crucial importance for high spatial resolution sensing. Therefore, further improvements require point defect sensors to be engineered closer to the surface or to be directly integrated into various low-dimensional structures. The currently available point defect qubit sensors in 3D semiconductors are not optimal for such applications due to their inherently bulk nature and strong dependence on surface chemistry[13–15]. The development of point defect qubits in layered van der Waals semiconductors may provide a way to overcome this obstacle as their surface is chemically stable, and the thickness of the host material, and thus the distance of the qubits and the surface, can be engineered straightforwardly by exfoliation[16–18]. Furthermore, van der Waals semiconductors with spin qubits can implement atomic thin sensors with advanced capabilities[16–21].

Hexagonal boron nitride (hBN) is a layered wide-bandgap semiconductor, which is often used in van der Waals heterostructures. Its large, close to 6 eV bandgap accommodates numerous optically active electronic states of structural defects and impurities[22,23]. Exfoliated hBN samples may contain point defects in such a low number that even individual color centers can be observed with confocal microscopy techniques. Numerous single photon emitters were demonstrated in hBN that has

opened a new field[22,24]. Point defect quantum bits form a special class of color centers that carry high-spin ground and optically excited states and feature a spin-dependent optical emission. This phenomenon makes optical detection of magnetic resonance (ODMR) measurements possible. ODMR signal of different spin qubits have already been reported[25–28] and predicted[29–32] in hBN.

One of the observed ODMR centers has been identified as the negatively charged boron vacancy center (VB⁻ center)[25,33–35]. The electronic, optical, and spin properties of the VB⁻ center has been comprehensively studied in the literature in numerous experimental[25,34–38] and theoretical studies[33,39–41]. While this center has already been successfully used in various sensing applications[16,17,19–21], single defect measurements have not been demonstrated yet, expectantly due to the center's low photoluminescence (PL) emission rate[33].

Identification of the atomic and electronic structure of other ODMR centers in hBN[26–28,42] is more challenging. In contrast to the VB⁻ center, these emitters are bright, can be measured at single defect level, and exhibit narrow ODMR lines[26–28,42]. These features make them interesting for quantum sensing applications[42]. Recently, it has been demonstrated that the formation of certain ODMR centers is directly related to carbon contamination in hBN[27]. Carbon impurities and related defects have been studied in numerous recent theoretical works[43–46]. Some of the investigated defects exhibit optical properties resembling the experimental signals[43,44], while others possess high-spin ground state[31,46].

Here, we theoretically study the neutral charge state of the nitrogen and the boron-centered symmetric carbon tetramer structures in hBN, i.e., $(C_B)^3$-C_N and $(C_N)^3$-C_B that we dub as C4N and C4B, respectively. The electronic structures of the defects consist of a triplet ground state, an optically allowed triplet excited state, and two singlet states between the triplets. For the C4B defect, we obtain a large intersystem crossing rate from the triplet excited state to the singlet manifold and a strain-dependent

¹Strongly Correlated Systems Lendület Research Group, Wigner Research Centre for Physics, PO Box 49, H-1525 Budapest, Hungary. ²MTA-ELTE Lendület "Momentum" NewQubit Research Group, Pázmány Péter, Sétány 1/A, 1117 Budapest, Hungary. ³Department of Chemical and Biological Engineering, The University of Alabama, Tuscaloosa, AL 35487, USA. ⁴Institute for Advanced Study, Technical University of Munich, Lichtenbergstrasse 2a, 85748 Garching, Germany. ⁵Department of Physics of Complex Systems, Eötvös Loránd University, Egyetem tér 1-3, H-1053 Budapest, Hungary. ⁶Department of Physics, Chemistry and Biology, Linköping University, SE-581 83 Linköping, Sweden. ✉email: barcza.gergely@wigner.hu; ivady.viktor@ttk.elte.hu

a C4N = $(C_B)^3$-C_N

b C4B = $(C_N)^3$-C_B

c

d
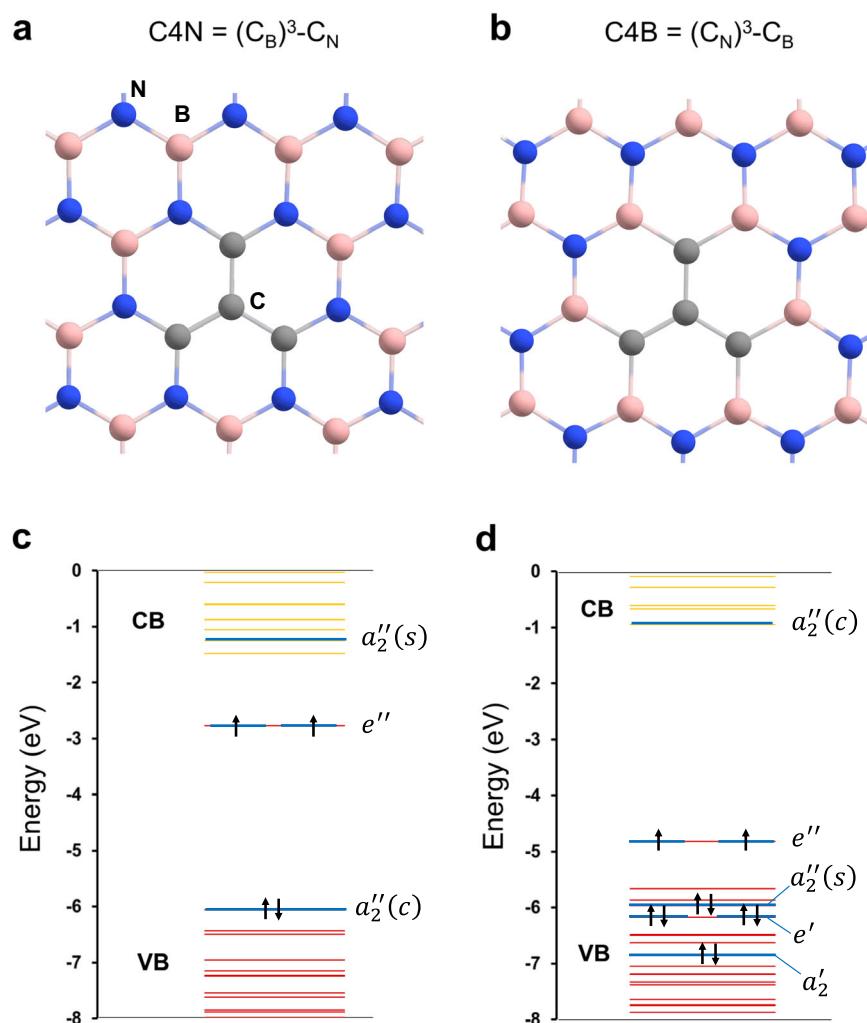
Fig. 1 Atomic and electronic structure of symmetric carbon tetramers in hBN. a, b shows the ground state atomic configuration of the nitrogen site-centered C4N defect and the boron site-centered C4B defect, respectively. Both defects exhibit D_{3h} point group symmetry. **c, d** depict the corresponding single-particle electronic structures. Yellow, red, and blue lines represent the conduction band, valence band, and defect energy levels, respectively. Up and down arrows indicate the occupation of the defect states. The localized defect orbitals are depicted in Supplementary Fig. 2.

intersystem crossing rate to the ground state. For the C4N defect, the spin selective decay is enabled by out-of-plane distortions. Therefore, strain can be used to engineer the defects' intersystem crossing rates and contrast. In addition, the carbon tetramers give rise to narrow magnetic resonance lines, due to the localization of the spin density on the spinless carbon atoms. Relying on our results, we propose the C4N and C4B defects in hBN as spin qubits for improving sensing in low dimensions.

The thermodynamic properties of carbon complexes have been studied recently in the literature[46,47]. Importantly, the symmetric C4N and C4B tetramers, see Fig. 1a, b, possess a surprisingly low formation energy. This can be explained by the Baird-aromatic stabilization of C4 containing hBN, i.e., there are two unpaired electrons and altogether $4k$ electrons in the delocalized π system of any selected set of rings; k denotes an arbitrary integer, which is similarly favorable to the Hückel aromaticity of pure hBN, i.e., there are $4k + 2$ electrons in the delocalized π system, all of which are paired. We note here that based on Baird's and Hückel's rules[48], the general conclusion can be drawn that an even number of carbon atoms can, while the odd number of carbon atoms cannot maintain aromaticity, implying larger formation energies in the latter case.

The formation energy of the neutral C4N and C4B defects are 2.5 eV (8.3 eV) and 8.7 eV (2.9 eV) in N-rich (B-rich) growth conditions and further decreases in charged configurations[46]. The most relevant charge transition levels are $E(++|+) = 2.38$ eV, $E(+|0) = 3.28$ eV, and $E(0|-) = 5.59$ eV for the C4N defect and $E(+|0) = 0.48$ eV, $E(0|-) = 3.03$ eV, and $E(-|--) = 3.90$ eV for the C4B defect measured from the valence band maximum[46]. The neutral charge state of the C4N (C4B) defect is thus stable in the upper half (lower half) of the bandgap, where the Fermi energy is located in N-rich (N-poor) growth conditions[46].

RESULTS

Single-particle levels

The single-particle electronic structures of the neutral ground state of the C4N and C4B defects are depicted in Fig. 1c, d, respectively. In-plane sp^2 bonding states of the atoms are fully occupied and most of them fall deep in the valence band. The four p_z orbitals of the carbon atoms form defect states that appear inside the bandgap. In the neutral charge state of the C4N defect, the most relevant single-particle defect states are the fully occupied $a_2''(c)$ state, the half occupied e'' states, and the empty
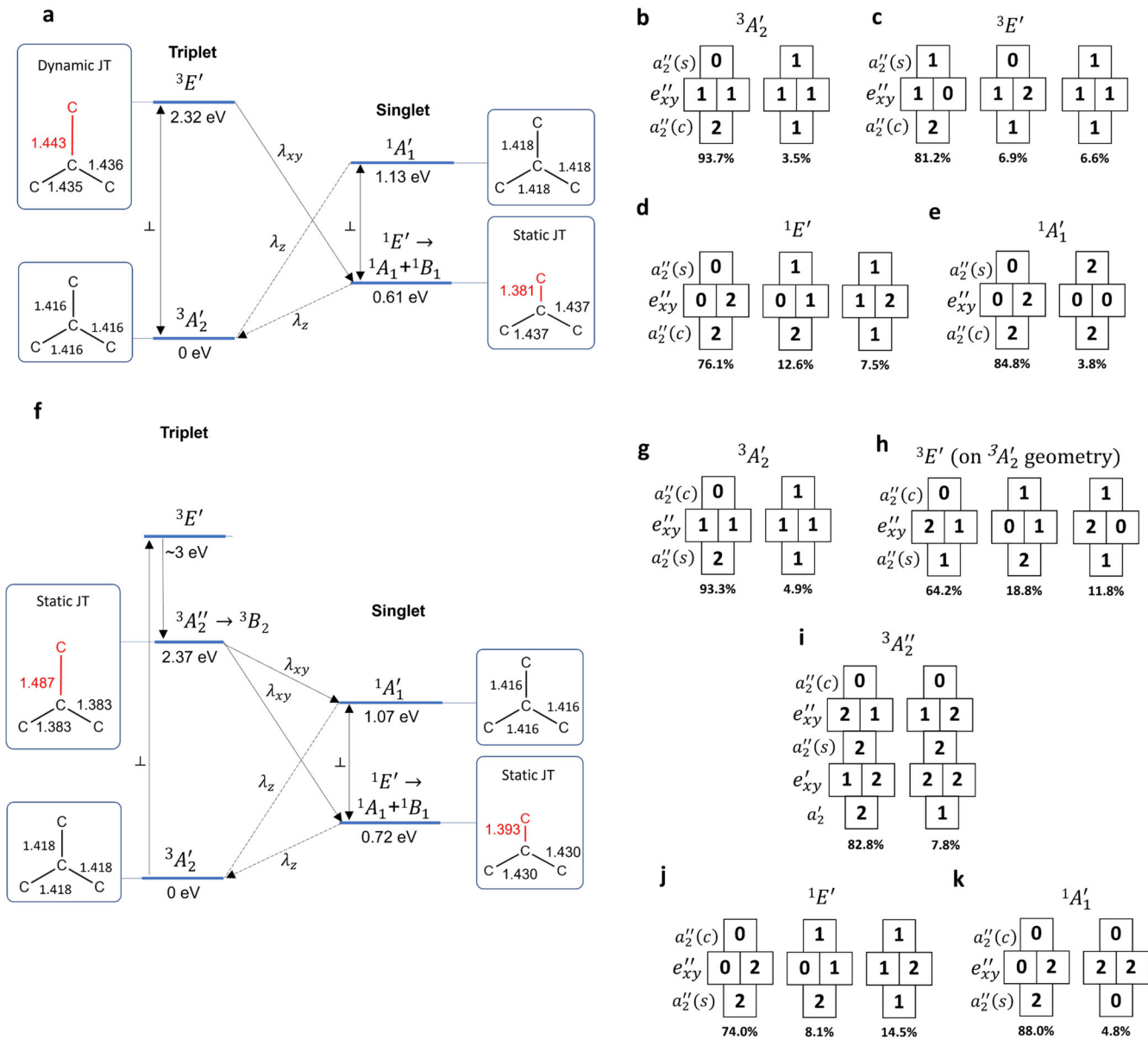
Fig. 2 Many-body electronic structure of the symmetric C4N and C4B defects. a Many-body spectrum of the C4N defect separated into singlet and triplet manifolds. The relative energy values are obtained at relaxed geometries without zero-point energy correction. Arrows connecting the states indicate possible optical and spin–orbit interaction-mediated non-radiative transitions. **b–e** Slater-determinant expression of the many-body states of the C4N defect. Squares with numbers indicate the occupancy of each of the localized defect states, while groups of squares represent different Slater determinants. The percentages below the Slater determinants represent the weight of the determinant in the expression. **f** Many-body spectrum of the C4B defect. The relative energy values are obtained at relaxed geometries without zero-point energy correction. **g–k** Slater-determinant expression of the many-body states of the C4B defect.

$a_2''(s)$, see Fig. 1c. As visualized in Supplementary Fig. 2, the a_2'' and e'' orbitals are primarily located on the central carbon atom and on the three side carbon atoms, respectively. $a_2''(c)$ orbital is strongly localized on the central carbon, while $a_2''(s)$ orbital is slightly delocalized and has significant contributions from the p_z orbitals of the surrounding three boron atoms. The most relevant defects states for the C4B defect are the fully occupied e' and $a_2''(s)$ states, the half occupied e'' state, and the empty $a_2''(c)$, see Fig. 1d and Supplementary Fig. 2. The occupied defect states of the C4B defect can be found closer to the valence band compared to the case of the C4N defect. For the C4B defect, a fully occupied in-plane bonding e' state can be found close to the valance band maximum and it plays an important role in the optical excitation process. Since the double degenerate e'' state is occupied by two

electrons with parallel spin, both defects exhibit a triplet ground state.

Low-energy excitation spectrum

The many-body electronic structures of the symmetric carbon tetramers, calculated after geometry relaxation for each electronic state, are schematically visualized in Fig. 2. The depicted energy gaps are obtained with an anticipated error margin of ±0.15 eV[49] on CASSCF-NEVPT2 level of theory[50]. As can be seen, four (five) states can be found in the low-energy part of the electronic structure of the C4N (C4B) defect. The ground states of both defects can be described to a large degree (>93%) by the single Slater determinant obtained in the single-particle picture in DFT, see Fig. 2c, d. For C4N, a $^3E'$ triplet state can be found 2.32 eV

above the $^3A_2'$ ground state. Note that the corresponding zero phonon photoluminescence (ZPL) energy, which is obtained by adding the zero-point energy contribution of the local vibrational modes to the 2.32 eV adiabatic energy difference, was found to be 2.18 eV. The $^3E'$ optically excited state is largely described by the determinant corresponding to the $e_x'' \rightarrow a_2''(s)$ transition, however, other determinants of single excitation mix with the leading term as depicted in Fig. 2c. The transition between the triplets is enabled by parallel to c polarized photon absorption and emission. The $^3E'$ state is Jahn–Teller (JT) unstable and the optimized structure is slightly distorted, see Fig. 2a. Due to the small JT distortion, we expect a dynamic Jahn–Teller effect, where the vibronic $^3\tilde{E}$ state exhibits effective high symmetry. Here, we note that an alternative, out-of-plane distorted triplet excited-state geometry was also observed in some calculations, see Supplementary Note 1. This effect is however peculiar to single, separated hBN layers. In-between the triplet states, there are two singlet excited states, a $^1E'$ state and a $^1A_1'$ state 0.61 eV and 1.13 eV above the ground state energy level, respectively.

For the C4B defect, we obtain a similar many-body electronic structure as for the C4N defect; however, with an additional dark triplet excited state in-between the ground state and the $^3E'$ triplet excited state, see Fig. 2f. The lower-lying $^3A_2''$ excited state and the optically excited $^3E'$ state is expected to be found 2.37 eV and ~3.0 eV above the ground state, respectively.

Note that in the exceptional case of C4B $^3E'$ state, the geometry relaxation turned out to be unfeasible due to the strong delocalization of the characteristic $a_2''(s)$ orbital. Thus, no geometrical data are shown for this state. Only the vertical excitation energy is available, which is 3.71 eV at $^3A_2'$ geometry. Of course, this data cannot be compared to the rest of the values in Fig. 2f. Still, it is possible to estimate the missing relaxation effects based on the closely related C4N $^3E'$ state, where a 0.62 eV energy decrease was observed. Altogether, this leads us to the aforementioned estimated energy level of $3.71 - 0.62 \approx 3$ eV for C4B $^3E'$.

The $^3A_2''$ and $^3E'$ states are described to a large degree by an $e' \rightarrow e''$ transition and $a_2' \rightarrow e''$ transition, respectively, see Fig. 2h and i. Both states are JT unstable and the point group symmetry of the optimized excited-state structure reduces to C_{2v}. The relaxed lowest energy triplet excited state belongs to the B_2 irreducible representation of C_{2v}. In D_{3h} symmetry, no optical transition is possible between the ground and the $^3A_2''$ excited state. This property is largely preserved even in the JT distorted $^3B_2''$ state. Transition to the higher-lying $^3E'$ state is possible, similarly to the C4N defect; however, due to the proximity of the $^3B_2''$ state a rapid non-radiative decay to this lower-lying triplet state is expected. Therefore, the C4B defect can be optically excited, but no PL emission is possible from this defect in the visible range. In addition to the triplets, we find two singlets, a $^1E'$ state and a $^1A_1'$ state 0.72 eV and 1.07 eV above the ground state, respectively.

Slater-determinant expansion of the singlet states are also provided in Fig. 2b–e and g–k for the C4N and C4B defects. The most relevant $^1E'$ and the $^1A_1'$ states are the singlets that correspond to the ground state occupancy of the single-particle orbitals. These singlets mix with other excited determinants to a similar degree as the optically excited states. The $^1E'$ state is a Jahn–Teller unstable state, and it goes through a severe structure distortion. In the optimized configuration one of the C–C bonds shortens that splits of the $^1E'$ state into a $^1A_1$ and a $^1B_1$ state in C_{2v} symmetry, see Fig. 2a, f.

Photoluminescence spectrum

After obtaining the $^3E' \rightarrow {}^3A_2'$ excitation energy (at state-average CASSCF-NEVPT2 level), the transition dipole moment (at state-average CASSCF-NEVPT2 level) and the harmonic vibrational modes of both ground and excited states (at time-dependent
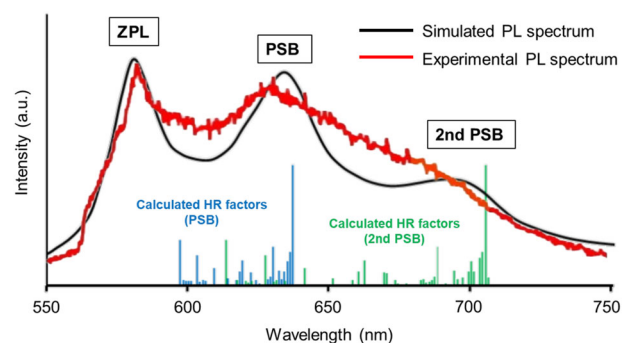
Fig. 3 Photoluminescence spectrum of the symmetric C4N defect in hBN compared with an experimental signal[27] of the unidentified carbon-related spin qubit in hBN. For better comparison, the theoretical ZPL emission is aligned with the first maximum of the experimental spectrum, where a shift of 0.06 eV is applied. The theoretical spectrum is also broadened to mimic temperature and inhomogeneous broadening effects. Blue and green impulses show the partial Huang–Rhys factors of one and two-photon processes.

(TD) DFT level), the calculation of excited-state dynamics, i.e., decay rates, Huang–Rhys factors, photon emission energies and intensities, based on the Golden Rule rate equation becomes straightforward and can be performed as a post-process. We note that both CASSCF-NEVPT2 and TD-DFT theories take all occupied valence band and empty conduction band states into account, as described in detail in the SI. For the radiative lifetime of the triplet excited states of the C4N defect, we obtain 80.5 ns at 0 K using a 2.13 refractive index for a 590 nm photon. The computed phonon sideband (PSB) of the C4N defect is visualized in Fig. 3. Herein, a line broadening of 300 cm^{-1} as well as a +0.06 eV shift is applied to the initially obtained spectrum to mimic the experimental results. We obtain 1.8 for the Huang–Rhys (HR) factor that corresponds to the Debye–Waller (DW) factor of 0.165. The relatively high DW factor for C4N defect is due to the high symmetry and small distortion of the excited-state geometry. In addition, in D_{3h} symmetry we expect weak coupling to electric field for the C4N structure[51].

Partial HR factors of the vibrational modes indicate that the PL transitions couple strongest to in-plane carbon-carbon bond stretching modes that drive the JT distorted excited state into the symmetric ground state configuration—see Supplementary Fig. 5 for the visualization of the vibrations. These modes are highly localized to carbon atoms, nevertheless, the B and N atoms of the lattice necessarily rearrange during the vibration to follow the $C_{2v} \rightleftarrows D_{3h}$ symmetry change of the C4 center. The energy of both modes is 0.196 eV (1583 cm^{-1}), which corresponds to the generally observed range of aromatic C–C stretching in infrared spectroscopy[52]. On the other hand, additional lower energy modes also couple to the defect that broadens and slightly shifts the maximum of the resonance peaks of the calculated PL spectrum. The phonon sideband of the PL emission of the C4N defect is compared with the experimental PL spectrum[27,28] of the unidentified carbon-related quantum bit, see Fig. 3. The theoretical and experimental spectra agree very well.

Point defect quantum bits are a special type of color centers that exhibit high-spin ground state and spin state-dependent optical emission through spin selective non-radiative decay processes from the optically excited state to the ground state. As carbon tetramers possess high-spin ground state and singlet shelving states between the triplet excited and ground states, they may implement optically addressable spin quantum bits in hBN that we investigate in the following.

In order to obtain an efficient spin state-dependent non-radiative decay channel through the singlets, the triplet, and the singlet manifolds should be coupled by strong spin–orbit coupling

Table 1. Spin–orbit coupling matrix elements (SOCMEs) as obtained on CASSCF-NEVPT2 level of theory for 0 K optimized and distorted atomic configurations.

C4N				C4B	
Transition	Matrix element			Transition	Matrix element 0 K static
	0 K static $(h/R = 0)$	Buckling $(h/R = 0.07)$	Buckling $(h/R = 0.18)$		
$^3E'(m_s = \pm1) \rightarrow {}^1A_1'$	0	16.03	31.95	$^3A_2''(m_s = \pm1) \rightarrow {}^1A_1'$	27.08
$^3E'(m_s = 0) \rightarrow {}^1A_1'$	0.03	0.03	0.18	$^3A_2''(m_s = 0) \rightarrow {}^1A_1'$	0
$^3E'(m_s = \pm1) \rightarrow {}^1E'$	0	7.67	13.26	$^3A_2''(m_s = \pm1) \rightarrow {}^1E'$	48.81
$^3E'(m_s = 0) \rightarrow {}^1E'$	0.45	4.65	14.94	$^3A_2''(m_s = 0) \rightarrow {}^1E'$	0
$^1A_1' \rightarrow {}^3A_2'(m_s = \pm1)$	0	0.26	0.15	$^1A_1' \rightarrow {}^3A_2'(m_s = \pm1)$	0
$^1A_1' \rightarrow {}^3A_2'(m_s = 0)$	2.76	2.61	11.25	$^1A_1' \rightarrow {}^3A_2'(m_s = 0)$	2.71
$^1E' \rightarrow {}^3A_2'(m_s = \pm1)$	0	6.41	9.53	$^1E' \rightarrow {}^3A_2'(m_s = \pm1)$	0
$^1E' \rightarrow {}^3A_2'(m_s = 0)$	0.27	0.24	1.47	$^1E' \rightarrow {}^3A_2'(m_s = 0)$	0.06

The bubble-like distortion is quantified by the ratio of bubble height and bubble half-width (h/R), see Supplementary Fig. 6 for the visualization of distorted geometries. All values are in GHz. We note that the matrix element depends on the geometry. Herein, the average of initial-state and final-state SOCMEs is given. When a zero and a nonzero SOCMEs are obtained for the involved initial and final electronic states, the nonzero value is provided.

(SOC) matrix elements. For the C4B defect, we obtain 48.81 GHz (27.08 GHz) spin–orbit coupling matrix elements between the $^3A_2''(m_S = \pm1)$ and the $^1E'$ ($^1A_1'$) states, see Table 1. Spin–orbit interaction thus gives rise to a decay channel with approximately 0.07 MHz decay rate for the dark excited triplet of the C4B defect. The spin–orbit coupling matrix elements between the $^1E'$ state and the ground state are weaker, enabled mostly by the Jahn–Teller distortion of the low-lying singlet state. Consequently, the $^1E'$ state is long-lived compared to the triplet excited state. These results indicate that the C4B defect can be spin polarized through an optical excitation to the $^3E'$ state and subsequent non-radiative and spin selective decay through the $^3A_2''$, $^1A_1'$, and $^1E'$ states. Due to this behavior, the C4B defect may be observed in electron spin resonance (ESR) measurement in low concentrations under ~3.0 eV excitation. In addition, due to the strict spin selectivity of the non-radiative decay from the $^3A_2''$ excited state and the expectedly long lifetime of the $^3A_2''(m_S = 0)$ state, the defect may be suitable for photoelectron-detected magnetic resonance (PDMR) readout of the spin states.

The C4N defect's lowest energy triplet excited state has a different symmetry than the excited state of the C4B defect, therefore, the spin–orbit coupling between the triplets and the singlets is forbidden in first-order approximation in D_{3h} symmetry. Indeed, considering the 0 K static atomic structure and corresponding many-particle electronic states, we obtain either zero or small spin–orbit coupling matrix elements between the states on CASSCF-NEVPT2 level of theory, see Table 1, left column. The nonzero elements are due to the JT effect yielding weak couplings between states. On the other hand, strain and out-of-plane distortions may break the symmetry that could give rise to a sizable increase in the spin–orbit coupling matrix elements for C4N. For example, in-plane compression of hBN flakes causes the sample to buckle and arrange to a bent configuration, which is similar to the experimentally observed hBN "bubbles"[53]. In such structures, the extent of out-of-plane distortion can be quantified by the ratio of bubble height (h) and bubble half-width (R)[54]. The h/R quotient equals to 0 in the equilibrium geometry as all atoms are located in one plane, but it shows an increasing deviation from 0 when enforcing the side of the flake—i.e., the outside B and N atoms - to remain in a fixed position closer and closer to the center, see Supplementary Fig. 6 for representative geometries and the visualization of geometrical parameters. Buckling of hBN, which is commonly observed in experiments[28], can lead to spin–orbit matrix elements in the 10–30 GHz range that are

comparable with NV center's matrix elements[55]. The increased SOC matrix elements give rise to spin-dependent non-radiative decay channels that may facilitate optical readout of the spin state.

As a demonstrative example, we compute the photoluminescence and intersystem crossing rates between the electronic states of a buckled flake at $h/R = 0.18$, see Supplementary Fig. 7. We note that the latter h/R ratio resembles an experimentally relevant bubble shape, as typical hBN bubbles possess a value of 0.1[54]. The obtained data indicate polarizability in $m_S = \pm1$ state. These results demonstrate that the C4N defect can implement an optically addressable spin qubit, whose spin-dependent optical signal is enabled mostly by local strain.

Apart from strain-induced geometry distortions, the out-of-plane vibration of the C4 center may also lead to significant SOC matrix elements, and hence intersystem crossing rates in the case of C4N. Namely, even though the matrix elements are zero (or close to zero) in equilibrium geometry, it does not hold true for non-equilibrium geometries where the system spends a significant amount of time due to its constant vibration—see Supplementary Note 2 for SOC matrix elements computed at geometries displaced along the out-of-plane normal mode. Thus, a Herzberg–Teller transition[56] is possible, the rate of which strongly depends on the occupancy of vibrational levels (i.e., the temperature).

Hyperfine structure

Next, we present our result on the spin properties of the C4N and C4B defects. For the zero-field splitting (ZFS) parameter D of the C4N defect, we obtain 820 MHz with CASSCF-NEVPT2. For the C4B defect, we obtain a slightly reduced $D = 660$ MHz ZFS value on CASSCF-NEVPT2 level of theory. Due to the D_{3h} symmetry, the quantization axis of the defects is parallel to the c axis, and no E splitting is observed in unstrained configurations. The spin density of the defects and the locations of the most relevant nuclear spins are depicted in Fig. 4a–c. The corresponding hyperfine coupling parameters, obtained with periodic hybrid-DFT in a bulk model, are provided in Table 2 and in Supplementary Table 6. Most notably, the spin density localizes mainly on the carbon atoms, and only secondary localization can be found on the first neighbor nitrogen atoms. Accordingly, the carbon hyperfine parameters are an order of magnitude larger than the rest of the coupling parameters. Using the theoretical spin coupling parameters, the
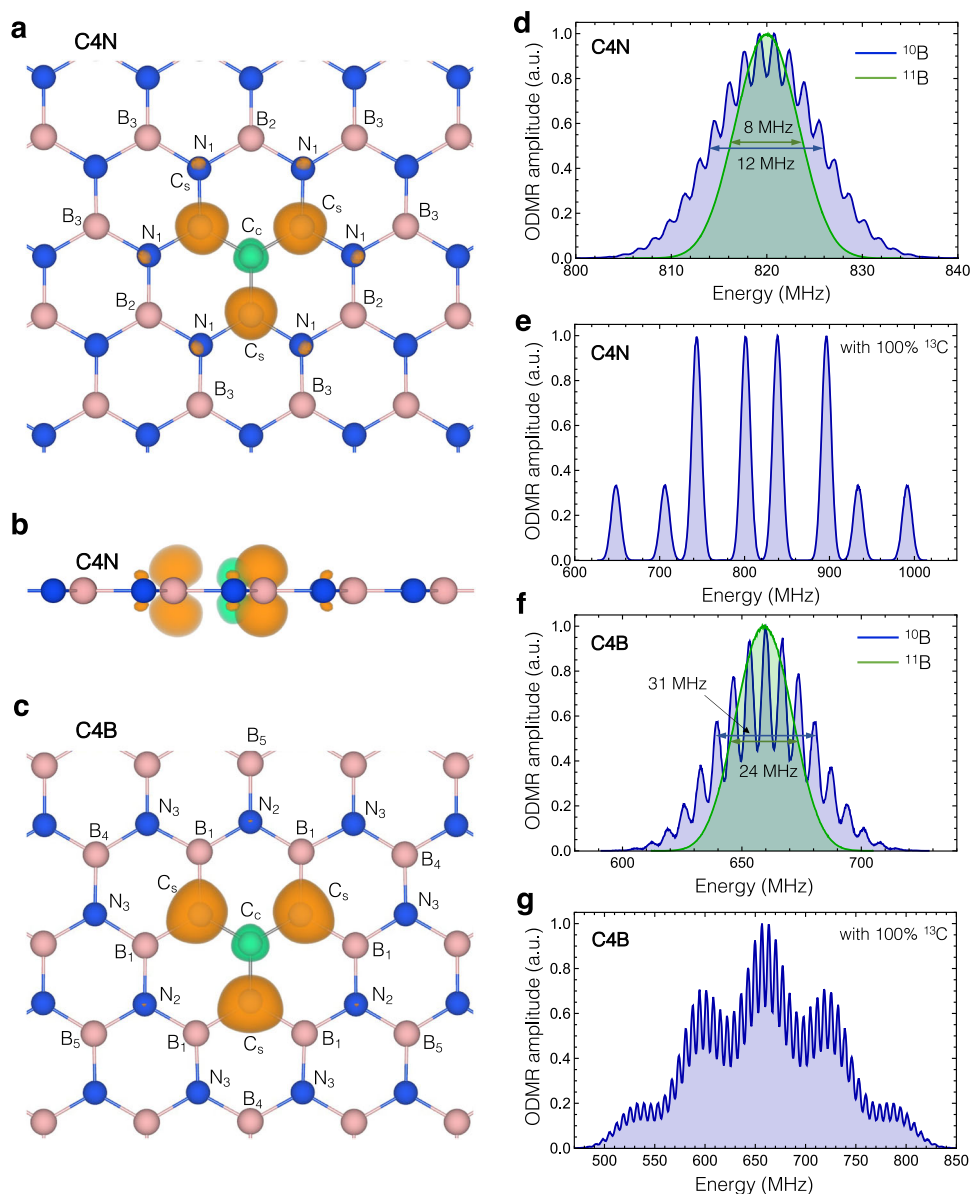
Fig. 4 Spin densities and spin resonance signals of symmetric carbon tetramers. a, b depict the spin density of the C4N defect from top and side views. **c** depicts the spin density of the C4B defect from the top view. **d** Electron spin resonance signal of the C4N defect at $B = 0$ with no carbon nuclear spins in ^{10}B (blue) and ^{11}B (green) containing samples. **e** Electron spin resonance signal of the C4N defect when it includes four ^{13}C nuclear spins. **f** Simulated electron spin resonance signal of the C4B defect with no carbon nuclear spins in ^{10}B and ^{11}B containing samples. **g** Electron spin resonance signal of the C4B defect, including four ^{13}C nuclear spins.

predicted electron spin resonance (ESR) spectra at zero magnetic fields for different isotope abundances are depicted in Fig. 4d–g. In natural abundance, ^{13}C nuclear spin can be found only with 1.07% probability, thus in most configurations, no carbon spins are included in the structures. When completely ignoring carbon nuclear spins, we obtain a narrow homogeneous ESR signal, where the linewidth is determined by the boron hyperfine coupling tensor and the boron isotope abundance. The full widths of the resonance peaks at half maximum are 12 MHz (8 MHz) and 31 MHz (24 MHz) for the C4N and the C4B defects in ^{10}BN (^{11}BN) sample. The narrow ESR linewidth may make the C4N and C4B defects attractive candidates for sensing. When carbon nuclear spins are included with 100% ^{13}C abundance, we observe a characteristic 8 peak hyperfine structure with 95.0 and 57.6 MHz splittings for the C4N defect, see Fig. 4e, and a characteristic 5 broad peak structure with ~60 MHz splitting for C4B defect, see Fig. 4g. ^{13}C-enriched carbon contamination and observation of the carbon-related

hyperfine structure can be used to unambiguously identify the C4N and C4B defects.

Chemical stability

Finally, we investigate the thermodynamic and kinetic stability of the C4N and C4B defects against complex formation with boron and carbon interstitial atoms. We observe that complex formation is energetically favorable and kinetically allowed in most of the cases, see Supplementary Note 3 for more details. The latter statement means that the highest energy barrier for complex formation is comparable to or even lower than the migration barrier of the interstitial atoms. Therefore, complex formation is limited by the availability and the migration of interstitial atoms. The only exception is the case of the C4N defect and the carbon interstitial atom. Here, we find a high energy barrier that can prevent complex formation up to ~630 K. We also estimate the

Table 2. Hyperfine tensors of C4N and C4B defect for the strongest coupled nuclear spins.

C4N						C4B					
Site	N	A_{xx}	A_{yy}	$A_{zz} = A_z$	A_{xy}	Site	N	A_{xx}	A_{yy}	$A_{zz} = A_z$	A_{xy}
C_c	1	−33.4	−33.4	−57.6	0.0	C_c	1	−22.9	−22.9	−48.0	0.0
C_s	3	8.6	8.8	95.0	0.0	C_s	3	−2.6	−2.6	68.9	0.0
N_1	6	−3.2	−3.3	0.3	0.1	B_1	6	−10.6	−8.5	−6.8	−0.2
B_2	3	−0.6	−0.3	1.7	0.0	N_2	3	−0.5	−0.3	1.5	0.0
B_3	6	0.2	−0.9	1.5	0.3	N_3	6	−0.1	−0.4	1.1	0.0
$B_{A/B}$	2	−0.3	−0.3	0.6	0.0	$B_{A/B}$	6	−0.2	−0.2	0.6	0.0

The location of the considered nuclear spins is visualized in Fig. 4. In the calculations, we use ^{13}C, ^{11}B, and ^{14}N isotopes. The table provides the hyperfine tensor for one of the symmetrically equivalent positions, and N gives the number of equivalent positions in the lattice. The complete table of hyperfine tensors can be found in Supplementary Table 6. All values are in MHz.

annealing temperature required to restore isolated C4N and C4B defects. The obtained annealing temperatures range between 690 and 1190 K. For comparison, we carry out a similar study for the VB− center in hBN, see Supplementary Note 3. As expected, the recombination of VB− center and interstitial atoms is highly favorable and practically irreversible, in contrast to the case of the C4N and C4B defects.

DISCUSSION

Recently, a few nanometers thick sensing foils have been developed by using spin qubit-containing hBN sheets[16–18]. We propose the charge-neutral symmetric carbon tetramers for implementing quantum bits in hBN. The narrow electron spin resonance linewidth of the nitrogen-centered carbon tetramer may lead to high sensitivity. Furthermore, the C4N and C4B spin qubits could also be highly beneficial for hBN-based dynamic nuclear polarization[38]. We show here that carbon tetramers can be spin polarized by optical illumination, leading to spin polarization sources that may couple to nuclear spins outside the hBN host. High-temperature and low-magnetic nuclear hyperpolarization mechanisms are long-time sought to boost the sensitivity of conventional NMR and MRI applications.

Previous computational studies[46] have demonstrated that carbon tetramers exhibit low formation energy in N-rich samples that may imply the formation of these complex defects in observable concentrations (~10^{14} cm$^{−3}$) in hBN. After growth treatments, however, may give rise to concentrations well exceeding the thermal equilibrium values and enable on-demand fabrication in few-layer samples. In this respect, carbon implantation might be of high importance with the potential to create carbon-related point defect quantum bits in hBN[27]. Furthermore, scanning transmission electron microscope (STEM) is also of high potential for sub-nanometer precision creation of defects[57]. STEM mapping combined with a subsequent annealing step allows the creation of the carbon complexes in single-layer hBN samples[57]. These processes open up new directions for tailored fabrication of carbon clusters, including the symmetric C4N defect, in hBN.

Finally, we discuss similarities and differences between the C4N defect and the not-yet-identified carbon-related single photon emitter and quantum bit in hBN that has been studied in numerous experimental reports lately[26–28,42,58,59]. As we have shown, the ZPL energy and the phonon sideband of the C4N defect and the unidentified qubit agree within the accuracy of our calculations, see Fig. 3. Furthermore, we predicted a narrow ESR linewidth for the C4N defect in natural hBN samples, which is also in agreement with the observed ~35 MHz ODMR linewidth of the carbon-related qubit defect[28]. An apparent difference between experiment and theory is, however, the value of the zero-field

splitting parameter D. In most cases, experimental extrapolations to zero magnetic field predict a vanishing D value, which suggests a doublet electron spin. Recently, this assumption has been unambiguously proven experimentally[59]. On the other hand, other recent experiments have reported a new ODMR signal of related emitters with a zero-field splitting parameter $D = 1.96$ GHz and in-plane quantization axis[42]. Using state-of-the-art theoretical methods, we could not explain these observations, thus the C4 defects are presumably not directly related to these ODMR centers.

In summary, we comprehensively studied the neutral nitrogen and boron site-centered symmetric carbon tetramers in hBN. By using complementary first-principles methods, we predicted the electronic structure as well as the optical and spin properties of the defects. We showed that symmetric carbon tetramers exhibit high-spin ground state, optical transition in the visible range, singlet shelving states, and strain-dependent non-radiative decay channels. We concluded that the C4N and C4B defects can implement spin qubits for sensing. Furthermore, we showed that strain can be used to tailor the spin contrast of the defects, which could broaden further the applicability of spin quantum bits in hBN.

METHODS

In this study, we carried out first-principles calculations of both periodic, supercell model, and molecule model of the symmetric C4 defects in hBN. The two approaches allowed independent computational studies on different levels of theory, ensuring the reliability of our results. Below we briefly summarize the computational protocols; the detailed description of the methodology as well as sample input files and the relaxed geometries for the sake of reproducibility can be found in the Supplementary Methods and Supplementary Notes 4 and 5, respectively.

Computations with supercell models

Kohn–Sham density functional theory was employed to study the periodic models of carbon tetramer defects with VASP package[60]. Here, we considered a plane wave basis set of 450 eV, PAW[61] core potentials, and HSE06 hybrid exchange-correlation functional[62] with 0.32 exact exchange fraction[63] (HSE(0.32)). The defects were modeled in 162-atom (monolayer) and 768-atom (bulk) supercells (Fig. 5, top). To account for van der Waals interaction, we included the D3 correction by Grimme et al.[64]. The ZPL energies were calculated from the energy difference between ground and excited states, where the excited states were obtained using spin-conserved constrained DFT method[65] without enforcing symmetry restrictions.
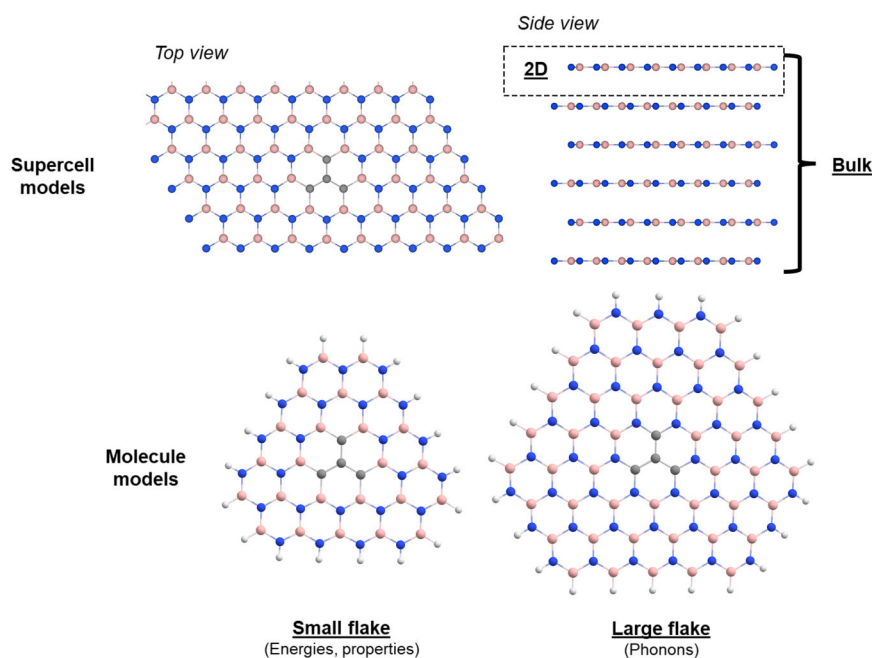
Fig. 5 Illustration of supercell and molecular models used in the present study for the case of C4N defect. The top left (right) panel shows the top view (side view) of the periodic supercell model used in the plane wave DFT simulations. The bottom left (right) panel shows the small (large) molecule model used in the quantum chemistry simulations.

Computations with molecule models

As a reasonable compromise between cost and accuracy, two hBN flakes of different sizes were used to investigate the C4 defects as a finite molecule. Electronic energies and properties, e.g., transition dipole moments, were computed on a smaller model (Fig. 5, bottom left), while phononic effects were calculated on a larger system (Fig. 5, bottom right). Test calculations justifying the choice of flake size can be found in the Supplementary Methods. All calculations were carried out using the ORCA 5.0.3. program[66].

Geometry optimizations and vibrational analyses were performed using density functional theory, at PBE0/cc-pVDZ level[67,68] with D3(BJ) dispersion correction[69]. In the case of excited states, time-dependent density functional theory (TD-DFT)[70] was requested with ten roots. Singlet excited states were generated from the triplet ground state by spin-flip[71].

Single-point energies and electronic properties were determined at CASSCF/cc-pVTZ level of theory[68,72] while dynamic correlation energy was taken into account by second-order N-electron valence perturbation theory (NEVPT2)[50]. The active orbital space for CASSCF was constructed based on both time-dependent density functional theory results obtained by ORCA and density matrix renormalization group (DMRG)[73–75] calculations using the Budapest-DMRG package[76].

Spin–orbit coupling (SOC) matrix elements, spin-spin coupling (SSC) and zero-field splitting tensors were calculated in the framework of the quasi-degenerate perturbation theory (QDPT)[77], in the basis of the obtained CASSCF roots. Convergence tests showed that the ZFS value obtained in the smallest molecule models is already convergent.

ESR spectrum calculations

In order to calculate the ESR line shape we implemented a fast Monte Carlo method. In the calculations, we randomly generate spin state configurations of the system and calculate the corresponding expectation value of the spin Hamiltonian. The states of the many-spin system are obtained as a tensor product of random S_z eigenstates of the considered spins. We considered the four carbon spins (when ^{13}C nuclear spins are considered) and the closest six nitrogen or boron nuclear spins. Including farther nuclear spins does not influence the shape of the ESR curve. When calculating the expectation values, we neglected off-diagonal elements of the Hamiltonian, which is a good approximation as long as the hyperfine mixing coupling terms are at least an order of magnitude smaller than the ZFS parameter D. After generating 2–10 million random states, the ESR spectrum is obtained as a histogram, which is proportional to the density of the states of the $m_S = \pm 1$ electron spin branch.

REFERENCES

1. Wang, Q. H., Kalantar-Zadeh, K., Kis, A., Coleman, J. N. & Strano, M. S. Electronics and optoelectronics of two-dimensional transition metal dichalcogenides. *Nat. Nanotechnol.* **7**, 699–712 (2012).
2. Manzeli, S., Ovchinnikov, D., Pasquier, D., Yazyev, O. V. & Kis, A. 2d transition metal dichalcogenides. *Nat. Rev. Mater.* **2**, 1–15 (2017).
3. Geim, A. K. & Grigorieva, I. V. Van der waals heterostructures. *Nature* **499**, 419–425 (2013).
4. Liang, S.-J., Cheng, B., Cui, X. & Miao, F. Van der Waals heterostructures for high-performance device applications: challenges and opportunities. *Adv. Mater.* **32**, 1903800 (2020).
5. Jelezko, F., Gaebel, T., Popa, I., Gruber, A. & Wrachtrup, J. Observation of coherent oscillations in a single electron spin. *Phys. Rev. Lett.* **92**, 076401 (2004).
6. Doherty, M. W. et al. The nitrogen-vacancy colour centre in diamond. *Phys. Rep.* **528**, 1 – 45 (2013).
7. Widmann, M. et al. Coherent control of single spins in silicon carbide at room temperature. *Nat. Mater.* **14**, 164–168 (2015).
8. Taylor, J. M. et al. High-sensitivity diamond magnetometer with nanoscale resolution. *Nat. Phys.* **4**, 810–816 (2008).

9. Schirhagl, R., Chang, K., Loretz, M. & Degen, C. L. Nitrogen-vacancy centers in diamond: nanoscale sensors for physics and biology. *Annu. Rev. Phys. Chem.* **65**, 83–105 (2014).

10. Barry, J. F. et al. Sensitivity optimization for NV-diamond magnetometry. *Rev. Mod. Phys.* **92**, 015004 (2020).

11. Stürner, F. M. et al. Integrated and portable magnetometer based on nitrogen-vacancy ensembles in diamond. *Adv. Quantum Technol.* **4**, 2000111 (2021).

12. Zhang, T. et al. Toward quantitative bio-sensing with nitrogen-vacancy center in diamond. *ACS Sens.* **6**, 2077–2107 (2021).

13. Kaviani, M. et al. Proper surface termination for luminescent near-surface NV centers in diamond. *Nano Lett.* **14**, 4772–4777 (2014).

14. Kim, M. et al. Decoherence of near-surface nitrogen-vacancy centers due to electric field noise. *Phys. Rev. Lett.* **115**, 087602 (2015).

15. Dwyer, B. L. et al. Probing spin dynamics on diamond surfaces using a single quantum sensor. *PRX Quantum* **3**, 040328 (2022).

16. Tetienne, J.-P. Quantum sensors go flat. *Nat. Phys.* **17**, 1074–1075 (2021).

17. Healey, A. J. et al. Quantum microscopy with van der Waals heterostructures. *Nat. Phys.* **19**, 87–91 (2023).

18. Kumar, P. et al. Magnetic imaging with spin defects in hexagonal boron nitride. *Phys. Rev. Appl.* **18**, L061002 (2022).

19. Gottscholl, A. et al. Spin defects in hBN as promising temperature, pressure and magnetic field quantum sensors. *Nat. Commun.* **12**, 4480 (2021).

20. Liu, W. et al. Temperature-dependent energy-level shifts of spin defects in hexagonal boron nitride. *ACS Photonics* **8**, 1889–1895 (2021).

21. Lyu, X. et al. Strain quantum sensing with spin defects in hexagonal boron nitride. *Nano Lett.* **22**, 6553–6559 (2022).

22. Caldwell, J. D. et al. Photonics with hexagonal boron nitride. *Nat. Rev. Mater.* **4**, 552–567 (2019).

23. Sajid, A., Ford, M. J. & Reimers, J. R. Single-photon emitters in hexagonal boron nitride: a review of progress. *Rep. Prog. Phys.* **83**, 044501 (2020).

24. Tran, T. T., Bray, K., Ford, M. J., Toth, M. & Aharonovich, I. Quantum emission from hexagonal boron nitride monolayers. *Nat. Nanotechnol.* **11**, 37–41 (2016).

25. Gottscholl, A. et al. Initialization and read-out of intrinsic spin defects in a van der Waals crystal at room temperature. *Nat. Mater.* **19**, 540–545 (2020).

26. Chejanovsky, N. et al. Single-spin resonance in a van der Waals embedded paramagnetic defect. *Nat. Mater.* **20**, 1079–1084 (2021).

27. Mendelson, N. et al. Identifying carbon as the source of visible single-photon emission from hexagonal boron nitride. *Nat. Mater.* **20**, 321–328 (2020).

28. Stern, H. L. et al. Room-temperature optically detected magnetic resonance of single defects in hexagonal boron nitride. *Nat. Commun.* **13**, 618 (2022).

29. Sajid, A. & Thygesen, K. S. VNCB defect as source of single photon emission from hexagonal boron nitride. *2D Mater.* **7**, 031007 (2020).

30. Babar, R. et al. Quantum sensor in a single layer van der Waals material. Preprint at http://arxiv.org/abs/2111.09589 (2021).

31. Bhang, J., Ma, H., Yim, D., Galli, G. & Seo, H. First-principles predictions of out-of-plane group IV and V dimers as high-symmetry, high-spin defects in hexagonal boron nitride. *ACS Appl. Mater. Interfaces* **13**, 45768–45777 (2021).

32. Liu, W. et al. Spin-active defects in hexagonal boron nitride. *Mater. Quantum Technol.* **2**, 032002 (2022).

33. Ivády, V. et al. Ab initio theory of the negatively charged boron vacancy qubit in hexagonal boron nitride. *NPJ Comput. Mater.* **6**, 1–6 (2020).

34. Haykal, A. et al. Decoherence of V_B^- spin defects in monoisotopic hexagonal boron nitride. *Nat. Commun.* **13**, 4347 (2022).

35. Liu, W. et al. Coherent dynamics of multi-spin V_B^- center in hexagonal boron nitride. *Nat. Commun.* **13**, 5713 (2022).

36. Gao, X. et al. High-contrast plasmonic-enhanced shallow spin defects in hexagonal boron nitride for quantum sensing. *Nano Lett.* **21**, 7708–7714 (2021).

37. Murzakhanov, F. F. et al. Electron-nuclear coherent coupling and nuclear spin readout through optically polarized VB- spin states in hBN. *Nano Lett.* **22**, 2718–2724 (2022).

38. Gao, X. et al. Nuclear spin polarization and control in hexagonal boron nitride. *Nat. Mater.* **21**, 1024–1028 (2022).

39. Sajid, A., Thygesen, K. S., Reimers, J. R. & Ford, M. J. Edge effects on optically detected magnetic resonance of vacancy defects in hexagonal boron nitride. *Commun. Phys.* **3**, 1–8 (2020).

40. Reimers, J. R. et al. Photoluminescence, photophysics, and photochemistry of the V_B^- defect in hexagonal boron nitride. *Phys. Rev. B* **102**, 144105 (2020).

41. Barcza, G. et al. DMRG on top of plane-wave Kohn-Sham orbitals: a case study of defected boron nitride. *J. Chem. Theory Comput.* **17**, 1143–1154 (2021).

42. Stern, H. L. et al. A quantum coherent spin in a two-dimensional material at room temperature. Preprint at http://arxiv.org/abs/2306.13025 (2023).

43. Jara, C. et al. First-principles identification of single photon emitters based on carbon clusters in hexagonal boron nitride. *J. Phys. Chem. A* **125**, 1325–1335 (2021).

44. Li, K., Smart, T. J. & Ping, Y. Carbon trimer as a 2 eV single-photon emitter candidate in hexagonal boron nitride: a first-principles study. *Phys. Rev. Mater.* **6**, L042201 (2022).

45. Golami, O. et al. Ab initio and group theoretical study of properties of a carbon trimer defect in hexagonal boron nitride. *Phys. Rev. B* **105**, 184101 (2022).

46. Maciaszek, M., Razinkovas, L. & Alkauskas, A. Thermodynamics of carbon point defects in hexagonal boron nitride. *Phys. Rev. Mater.* **6**, 014005 (2022).

47. Huang, P. et al. Carbon and vacancy centers in hexagonal boron nitride. *Phys. Rev. B* **106**, 014107 (2022).

48. Sung, Y. M. et al. Reversal of Hückel (anti)aromaticity in the lowest triplet states of hexaphyrins and spectroscopic evidence for Baird's rule. *Nat. Chem.* **7**, 418–422 (2015).

49. Sarkar, R., Loos, P.-F., Boggio-Pasqua, M. & Jacquemin, D. Assessing the performances of CASPT2 and NEVPT2 for vertical excitation energies. *J. Chem. Theory Comput.* **18**, 2418–2436 (2022).

50. Angeli, C., Cimiraglia, R., Evangelisti, S., Leininger, T. & Malrieu, J.-P. Introduction of n-electron valence states for multireference perturbation theory. *J. Chem. Phys.* **114**, 10252–10264 (2001).

51. Zhigulin, I. et al. Stark effect of blue quantum emitters in hexagonal boron nitride. *Phys. Rev. Appl.* **19**, 044011 (2023).

52. Lin-Vien, D., Colthup, N. B., Fateley, W. G. & Grasselli, J. G. Chapter 17—aromatic and heteroaromatic rings. in *The Handbook of Infrared and Raman Characteristic Frequencies of Organic Molecules* (eds Lin-Vien, D. et al.) 277–306 (Academic Press, 1991).

53. He, L. et al. Isolating hydrogen in hexagonal boron nitride bubbles by a plasma treatment. *Nat. Commun.* **10**, 2815 (2019).

54. Blundo, E. et al. Vibrational properties in highly strained hexagonal boron nitride bubbles. *Nano Lett.* **22**, 1525–1533 (2022).

55. Thiering, G. & Gali, A. Ab initio calculation of spin-orbit coupling for an NV center in diamond exhibiting dynamic Jahn-Teller effect. *Phys. Rev. B* **96**, 081115 (2017).

56. Manian, A., Shaw, R. A., Lyskov, I., Wong, W. & Russo, S. P. Modeling radiative and non-radiative pathways at both the Franck-Condon and Herzberg-Teller approximation level. *J. Chem. Phys.* **155**, 054108 (2021).

57. Park, H. et al. Atomically precise control of carbon insertion into hBN monolayer point vacancies using a focused electron beam guide. *Small* **17**, 2100693 (2021).

58. Guo, N.-J. et al. Coherent control of an ultrabright single spin in hexagonal boron nitride at room temperature. *Nat. Commun.* **14**, 2893 (2023).

59. Scholten, S. C. et al. Multi-species optically addressable spin defects in a van der Waals material. Preprint at http://arxiv.org/abs/2306.16600. (2023).

60. Kresse, G. & Hafner, J. Ab initio molecular-dynamics simulation of the liquid-metal-amorphous-semiconductor transition in germanium. *Phys. Rev. B* **49**, 14251–14269 (1994).

61. Blöchl, P. E. Projector augmented-wave method. *Phys. Rev. B* **50**, 17953–17979 (1994).

62. Heyd, J., Scuseria, G. E. & Ernzerhof, M. Hybrid functionals based on a screened coulomb potential. *J. Chem. Phys.* **118**, 8207 (2003).

63. Weston, L., Wickramaratne, D. & Van de Walle, C. G. Hole polarons and p-type doping in boron nitride polymorphs. *Phys. Rev. B* **96**, 100102 (2017).

64. Grimme, S., Antony, J., Ehrlich, S. & Krieg, H. A consistent and accurate ab initio parametrization of density functional dispersion correction (DFT-D) for the 94 elements H-Pu. *J. Chem. Phys.* **132**, 154104 (2010).

65. Gali, A., Janzén, E., Deák, P., Kresse, G. & Kaxiras, E. Theory of spin-conserving excitation of the $N-V^-$ center in diamond. *Phys. Rev. Lett.* **103**, 186404 (2009).

66. Neese, F. Software update: the ORCA program system-version 5.0. *Wiley Interdiscip. Rev. Comput. Mol. Sci.* **12**, e1606 (2022).

67. Adamo, C. & Barone, V. Toward reliable density functional methods without adjustable parameters: the PBE0 model. *J. Chem. Phys.* **110**, 6158–6170 (1999).

68. Dunning, T. H. Gaussian basis sets for use in correlated molecular calculations. i. the atoms boron through neon and hydrogen. *J. Chem. Phys.* **90**, 1007–1023 (1989).

69. Grimme, S., Ehrlich, S. & Goerigk, L. Effect of the damping function in dispersion corrected density functional theory. *J. Comput. Chem.* **32**, 1456–1465 (2011).

70. Neese, F. Prediction of molecular properties and molecular spectroscopy with density functional theory: from fundamental theory to exchange-coupling. *Coord. Chem. Rev.* . **253**, 526–563 (2009).

71. Casanova, D. & Krylov, A. I. Spin-flip methods in quantum chemistry. *Phys. Chem. Chem. Phys.* **22**, 4326–4342 (2020).

72. Kollmar, C., Sivalingam, K., Helmich-Paris, B., Angeli, C. & Neese, F. A perturbation-based super-ci approach for the orbital optimization of a CASSCF wave function. *J. Comput. Chem.* **40**, 1463–1470 (2019).

73. White, S. R. & Martin, R. L. Ab initio quantum chemistry using the density matrix renormalization group. *J. Chem. Phys.* **110**, 4127–4130 (1999).

74. Szalay, S. et al. Tensor product methods and entanglement optimization for ab initio quantum chemistry. *Int. J. Quantum. Chem.* **115**, 1342–1391 (2015).

75. Freitag, L. & Reiher, M. In *The Density Matrix Renormalization Group for Strong Correlation in Ground and Excited States*, (eds González, L. & Lindh, R.) Chap. 7, 205–245 (John Wiley and Sons, Ltd, 2020).

76. Legeza, Ö., Veis, L. & Mosoni, T. QC-DMRG-Budapest, a program for quantum chemical DMRG calculations.

77. Ganyushin, D. & Neese, F. First-principles calculations of zero-field splitting parameters. *J. Chem. Phys.* **125**, 024103 (2006).

AUTHOR CONTRIBUTIONS

Z.B., R.B., A.G., and G.B. carried out the first-principles calculations, O.L. developed the DMRG program package. V.I., Z.B., and G.B. wrote the manuscript with inputs from all coauthors. The work was supervised by V.I. and G.B.

COMPETING INTERESTS

The authors declare no competing interests.

ADDITIONAL INFORMATION

Supplementary information The online version contains supplementary material available at https://doi.org/10.1038/s41524-023-01135-z.

Correspondence and requests for materials should be addressed to Gergely Barcza or Viktor Ivády.

Reprints and permission information is available at http://www.nature.com/reprints

Publisher's note Springer Nature remains neutral with regard to jurisdictional claims in published maps and institutional affiliations.